

Spectrally engineered photonic molecules as optical sensors with enhanced sensitivity: a proposal and numerical analysis

Svetlana V. Boriskina

School of Radiophysics, V. Karazin Kharkov National University, Kharkov 61077, Ukraine

Received January 25, 2006; revised March 21, 2006; accepted March 25, 2006; posted March 28, 2006 (Doc. ID 67434)

We report a theoretical study of clusters of evanescently coupled 2D whispering-gallery mode optical microcavities (termed “photonic molecules”) as chemosensing and biosensing platforms. Photonic molecules (PMs) supporting modes with narrow linewidths, wide mode spacing, and greatly enhanced sensitivity to the changes in the dielectric constant of their environment and to the presence of individual subwavelength-sized nanoparticles in the PM evanescent-field region are numerically designed. This type of optical biosensor can be fabricated in a variety of material platforms and integrated on a single chip that makes it a promising candidate for a small and robust laboratory-on-a-chip device. Possible applications of the developed methodology and the designed PM structures to near-field microscopy, single nanoemitter microcavity lasing, and cavity-controlled single-molecule fluorescence enhancement are also discussed. © 2006 Optical Society of America

OCIS codes: 130.3120, 230.5750, 140.4780, 130.6010.

1. INTRODUCTION

The growing need for miniaturized instruments for medical, food, and environmental testing together with the rising level of bioterrorism concerns have fueled the development of optical biosensors. Optical microcavities (microdisks and microspheres) supporting high- Q whispering-gallery (WG) modes (with light confined near the resonator surface by almost total internal reflection) have already been demonstrated to have great potential in the development of inexpensive, ultracompact, highly sensitive, and robust biosensors and chemical sensors.^{1–9} As compared with more traditional linear optical waveguides or fiber biosensors, microresonator-based devices benefit from a much smaller size (several micrometers rather than a few centimeters) and higher sensitivity. Optical resonators enable a significant decrease of the analyte sample needed for efficient sensing.

Two basic sensing principles are usually employed in microresonator-based optical sensors. The first class of sensors is designed to detect the resonant frequency shift caused by the change of the refractive index of the surrounding environment through the interaction of the evanescent field of the WG mode outside the microcavity with the biochemical agent (mass sensing).^{2–8} This refractive index change can be caused by the change of the concentration of bio(chemical) material on the resonator surface or in the surrounding solution. Detection can also be made by measuring the output intensity change from the microresonator at a fixed wavelength. The other class of devices uses the evanescent field of the microresonator to excite the spectroscopic (fluorescence or Raman) signal from the molecules of the analyte (fluorescence sensing).^{9,10} In both methods, high- Q factors (narrow resonant linewidths and long-cavity decay lifetimes) of the resonator modes are crucial for achieving high-sensor sensitivity.

Microdisk resonators offer certain advantages over microspheres for use as biosensors, as they can be fabricated with standard microfabrication technologies and easily integrated with other components and bus waveguides on a semiconductor chip. However, similar to the case of microspheres, there are several factors that may hinder the use of WG-mode circular microdisk resonators as sensitive and robust biosensing platforms. First, for a high- Q WG mode in a single microdisk, the interaction of the evanescent-mode field with the analyte is weak due to high confinement of the modal field inside the resonator. Furthermore, the wavelength spacing between high- Q WG modes in optically large cavities becomes so small that the individual modes cannot be resolved. These modes form a relatively broad peak in a measured cavity spectrum,⁸ making efficient detection difficult. On the other hand, widely spaced WG modes supported by wavelength-scale nanocavities have low- Q factors whose values decrease exponentially with a decreased mode azimuthal order.¹¹ The symmetry of circular microdisks also results in double degeneracy of the WG modes that they support [corresponding to the mode angular-field dependence $\cos(m\varphi)$ or $\sin(m\varphi)$]. This degeneracy is often removed by fabrication imperfections that break the symmetry of the structure and cause the appearance of parasitic peaks in the resonator spectra.¹²

To overcome the aforementioned limitations, we suggest using clusters of coupled nanocavities (photonic molecules)¹³ with a wide free-spectral range tuned to a symmetry-enhanced high- Q WG mode resonance¹⁴ instead of a larger single microcavity. Properly designed photonic molecules (PMs) have already demonstrated a high potential for the design of low-threshold microlasers.^{14–17} In a previous publication,¹⁴ I showed that by arranging circular WG-mode microcavities into predesigned symmetrical configurations it is possible to

not only preserve but also significantly enhance their attractive features, such as the high- Q factors, and simultaneously remove the obstacles hindering their use, namely, the WG-mode double degeneracy. In this work, for the first time to my knowledge, it is shown (through 2D numerical simulations based on the rigorous integral-equation method presented here) that optimally tuned PMs also demonstrate significant enhancement of the sensitivity to the changes in their environment. Furthermore, I demonstrate that arranging such PMs into symmetrical “supermolecules” results in an even further enhancement of their Q factors and sensitivity, paving the way for their use as sensitive nanoscale biochemical sensors on a chip. Finally I show that such PMs also enable the detection of individual nanoparticles with the sizes below the diffraction limit.

2. PROBLEM GEOMETRY AND METHODOLOGY

PMs composed of several evanescently coupled microcavities supporting high- Q WG modes play an important role in photonics research, as they can potentially find use for various applications ranging from optical power transfer via coupled-resonator optical waveguides to low-threshold PM microlasers. A PM composed of L side-coupled micro-disk resonators is considered as illustrated in Fig. 1. The dielectric (or semiconductor) microdisks of radii a_ℓ , and permittivities ε_ℓ ($\ell=1, \dots, L$) are located in a host medium with permittivity ε_e .

For thin disks, the 3D problem of finding the eigenfrequencies of the PM can be replaced with an equivalent 2D formulation by using the effective-index method to account for the vertical field confinement (the disk permittivities should then be replaced with their corresponding effective values).¹⁸ In the rest of this paper, we will thus restrict ourselves to simplified 2D calculations. The effective refractive index of the disks used in the following sections ($n_{\text{eff}}=2.63$) may correspond to, e.g., air-clad 165 nm thick silicon disks ($n=3.52$) located on a silica substrate ($n=1.444$) or 200 nm thick InGaAsP disks ($n=3.37$) suspended in the air at 1550 nm. To account for the material

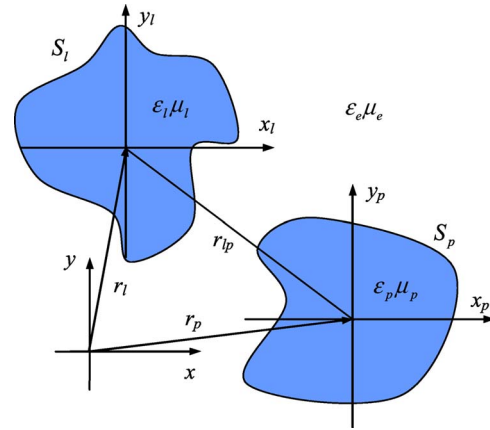


Fig. 1. (Color online) Schematic of a coupled-microdisk cluster immersed into a homogeneous dielectric medium.

losses in the cavity, we also assume a small positive value of the imaginary part of the cavity effective dielectric constant ($\varepsilon_{\text{eff}}=6.9169+i10^{-4}$). Applying the Green's formula to the fields (U_ℓ) and the Green's functions in the regions inside (G_ℓ^c) and outside (G_ℓ^e) all the microcavities and taking into account the transparency conditions at the cavity boundaries, we can formulate the problem in terms of the 2D Muller boundary integral equations (MBIEs)¹⁸:

$$\begin{aligned}
 U_p(\mathbf{r}) = U^{\text{inc}}(\mathbf{r}) + \sum_{\ell=1}^L \int_{s_\ell} \left\{ U_\ell(\mathbf{r}') \frac{\partial}{\partial n'} [G_\ell^c(\mathbf{r}, \mathbf{r}') - G_\ell^e(\mathbf{r}, \mathbf{r}')] \right. \\
 \left. - V_\ell(\mathbf{r}') \left[G_\ell^c(\mathbf{r}, \mathbf{r}') - \frac{\alpha_e}{\alpha_\ell} G_\ell^e(\mathbf{r}, \mathbf{r}') \right] \right\} ds'_\ell, \\
 \frac{\alpha_e + \alpha_p}{2\alpha_p} V_p(\mathbf{r}) = V^{\text{inc}}(\mathbf{r}) + \sum_{\ell=1}^L \int_{s_\ell} \left\{ U_\ell(\mathbf{r}') \frac{\partial^2}{\partial n \partial n'} [G_\ell^c(\mathbf{r}, \mathbf{r}') \right. \\
 \left. - G_\ell^e(\mathbf{r}, \mathbf{r}')] - V_\ell(\mathbf{r}') \frac{\partial}{\partial n} \left[G_\ell^c(\mathbf{r}, \mathbf{r}') \right. \right. \\
 \left. \left. - \frac{\alpha_e}{\alpha_\ell} G_\ell^e(\mathbf{r}, \mathbf{r}') \right] \right\} ds'_\ell, \quad (1)
 \end{aligned}$$

where $p=1, \dots, L$ (L being a total number of cavities), and

$$\begin{aligned}
 U_\ell^{\text{TE}}(\mathbf{r}) = H_z^\ell(\mathbf{r}), \quad V_\ell^{\text{TE}}(\mathbf{r}) = \frac{\partial H_z^\ell(\mathbf{r})}{\partial n}, \quad \alpha_\ell = \varepsilon_\ell, \quad \alpha_e = \varepsilon_e, \\
 U_\ell^{\text{TM}}(\mathbf{r}) = E_z^\ell(\mathbf{r}), \quad V_\ell^{\text{TM}}(\mathbf{r}) = \frac{\partial E_z^\ell(\mathbf{r})}{\partial n}, \quad \alpha_\ell = \mu_\ell, \quad \alpha_e = \mu_e, \\
 \ell = 1, \dots, L. \quad (2)
 \end{aligned}$$

Note that the analytical procedure developed here for the case of L electromagnetically coupled microcavities is a generalization of the solution for a single isolated microcavity.¹⁸ Equations (1) are the Fredholm second-kind integral equations with either smooth or integrable kernels and are free of spurious solutions. Thus their discretization yields well-conditioned matrices.¹⁸

Note that Eqs. (1) are valid for microdisks of arbitrary smooth cross sections. As the next step of the solution procedure, we shall obtain a discretized form of the MBIEs for a specific (and important for a number of practical applications) case of L coupled circular microdisks of different radii a_ℓ . The expressions for the Green's functions for the case of source point Q located inside and observation

point P located either inside or outside of the p th micro-cavity of radius a_p and permittivity ε_p immersed into a host medium with permittivity ε_e can be written in the coordinate system associated with the p th cavity as follows [see Fig. 2(a)]:

$$G_p^c(\mathbf{r}, \mathbf{r}') = \frac{i}{4} \sum_{(m)} J_m[k_p r_p(P)] H_m^{(1)}[k_p r_p(Q)] \times \exp[-im\theta_p(Q)] \exp[im\theta_p(P)], \quad r_p(P) \leq r_p(Q),$$

$$G_p^e(\mathbf{r}, \mathbf{r}') = \frac{i}{4} \sum_{(m)} J_m[k_e r_p(Q)] H_m^{(1)}[k_e r_p(P)] \times \exp[-im\theta_p(Q)] \exp[im\theta_p(P)], \quad r_p(P) \geq r_p(Q). \quad (3)$$

However, if source point Q is located inside the ℓ th cavity (of radius a_ℓ and permittivity ε_ℓ) and observation point P is located either inside the p th cavity or in the outer region, the Green's functions take the following forms in the local coordinate system associated with the ℓ th cavity [see Fig. 2(b)]:

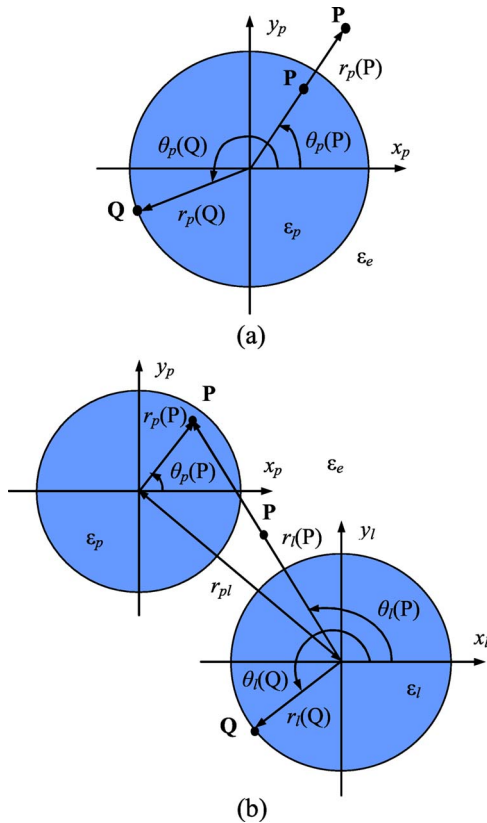


Fig. 2. (Color online) Two possible locations of the source (Q) and the observation (P) points in the expressions for the Green's functions; (a) both points belong to the same cavity and (b) the points belong to different cavities. The global and local coordinate systems used in the analysis are also shown.

$$G_\ell^c(\mathbf{r}, \mathbf{r}') = \frac{i}{4} \sum_{(m)} J_m[k_\ell r_\ell(Q)] H_m^{(1)}[k_\ell r_\ell(P)] \times \exp[-im\theta_\ell(Q)] \exp[im\theta_\ell(P)], \quad r_\ell(P) \geq r_\ell(Q),$$

$$G_\ell^e(\mathbf{r}, \mathbf{r}') = \frac{i}{4} \sum_{(m)} J_m[k_e r_\ell(Q)] H_m^{(1)}[k_e r_\ell(P)] \times \exp[-im\theta_\ell(Q)] \exp[im\theta_\ell(P)], \quad r_\ell(P) \geq r_\ell(Q). \quad (4)$$

By using the following Graf's formulas for the Hankel functions,^{19,20} Eqs. (4) can be rewritten in a more convenient form, where the coordinates of point P are given in the p th coordinate system:

$$H_m^{(1)}[kr_\ell(P)] \exp[im\theta_\ell(P)] = \sum_{(n)} H_{n-m}^{(1)}(kr_p\ell) J_n[kr_p(P)] \times \exp[i(m-n)\theta_p^\ell] \exp[in\theta_p(P)], \quad r_p(P) < r_{p\ell},$$

$$H_m^{(1)}[kr_\ell(P)] \exp[im\theta_\ell(P)] = \sum_{(n)} J_{n-m}(kr_p\ell) H_n^{(1)}[kr_p(P)] \times \exp[i(m-n)\theta_p^\ell] \exp[in\theta_p(P)], \quad r_p(P) > r_{p\ell}. \quad (5)$$

Now we substitute the above expressions into the MBIEs [Eqs. (1)] and expand the unknown functions in terms of the Fourier series with angular exponents as global basis functions. Testing against the same set of global functions yields the final matrix equation that needs to be solved to determine the unknown Fourier coefficients u_m^p and v_m^p :

$$a_m^p u_m^p + b_m^p v_m^p + \sum_{\ell \neq p} \left\{ \sum_{(n)} u_n^\ell A_{mn} + \sum_{(n)} v_n^\ell B_{mn} \right\} = 0,$$

$$c_m^p u_m^p + d_m^p v_m^p + \sum_{\ell \neq p} \left\{ \sum_{(n)} u_n^\ell C_{mn} + \sum_{(n)} v_n^\ell D_{mn} \right\} = 0, \quad (6)$$

where

$$a_m^p = \sqrt{\varepsilon_p} J_m(k_p a_p) H_m^{(1)'}(k_p a_p) - \sqrt{\varepsilon_e} J_m'(k_e a_p) H_m^{(1)}(k_e a_p) + \frac{4}{i\pi k a_p},$$

$$b_m^p = J_m(k_p a_p) H_m^{(1)}(k_p a_p) - \frac{\alpha_e}{\alpha_p} J_m(k_e a_p) H_m^{(1)}(k_e a_p),$$

$$c_m^p = \varepsilon_e J_m'(k_e a_p) H_m^{(1)'}(k_e a_p) - \varepsilon_p J_m'(k_p a_p) H_m^{(1)'}(k_p a_p),$$

$$d_m^p = \frac{\alpha_e}{\alpha_p} \sqrt{\varepsilon_e} J_m(k_e a_p) H_m^{(1)'}(k_e a_p) - \sqrt{\varepsilon_p} J_m'(k_p a_p) H_m^{(1)}(k_p a_p) + \frac{2(\alpha_p + \alpha_e)}{i\pi\alpha_p k a_p},$$

$$A_{mn} = [\sqrt{\varepsilon_\ell} J_n'(k_\ell a_\ell) J_m(k_\ell a_p) H_{m-n}^{(1)}(k_\ell r_{p\ell}) - \sqrt{\varepsilon_e} J_n'(k_e a_\ell) J_m(k_e a_p) H_{m-n}^{(1)}(k_e r_{p\ell})] e^{i(n-m)\theta_p^\ell},$$

$$B_{mn} = \left[J_n(k_\ell a_\ell) J_m(k_\ell a_p) H_{m-n}^{(1)}(k_\ell r_{p\ell}) - \frac{\alpha_e}{\alpha_\ell} J_n(k_e a_\ell) J_m(k_e a_p) H_{m-n}^{(1)}(k_e r_{p\ell}) \right] e^{i(n-m)\theta_p^\ell},$$

$$C_{mn} = [\varepsilon_e J_n'(k_e a_\ell) J_m'(k_e a_p) H_{m-n}^{(1)}(k_e r_{p\ell}) - \varepsilon_\ell J_n'(k_\ell a_\ell) J_m'(k_\ell a_p) H_{m-n}^{(1)}(k_\ell r_{p\ell})] e^{i(n-m)\theta_p^\ell},$$

$$D_{mn} = \left[\frac{\alpha_e}{\alpha_\ell} \sqrt{\varepsilon_e} J_n(k_e a_\ell) J_m'(k_e a_p) H_{m-n}^{(1)}(k_e r_{p\ell}) - \sqrt{\varepsilon_\ell} J_n(k_\ell a_\ell) J_m'(k_\ell a_p) H_{m-n}^{(1)}(k_\ell r_{p\ell}) \right] e^{i(n-m)\theta_p^\ell}.$$

Coefficients $a_m - d_m$ of Eqs. (6) correspond to the matrix coefficients of a problem for an isolated p th cavity, while coefficients $A_{mn} - D_{mn}$ describe the optical coupling between the p th and the ℓ th cavities. It should be noted here that if several microcavities are arranged in a PM with the intercavity spacing comparable with the cavity sizes and the optical wavelength, these coefficients play a very important role in the numerical solution, as mutual electromagnetic interactions inside the structure can drastically affect its optical properties. Such PMs support collective supermodes, whose frequencies and Q factors may vary significantly from those of a single microcavity. The algorithm presented here yields analytical expressions for all the matrix coefficients, and thus provides superior accuracy of numerical solutions.

Homogeneous Eqs. (6) have nonzero solutions only at frequencies where the equation matrix becomes singular. Complex eigenfrequencies of the optical modes supported by a set of coupled resonators are found by searching for the roots of the matrix determinant in the complex frequency plane. Once the eigenfrequencies are found, the modal fields and emission characteristics can be calculated by solving the homogeneous matrix Eqs. (6) at the eigenfrequencies. In the frame of the 2D model, the numerical results are exact up to the truncation error of the angular Fourier series and up to the accuracy of the root searching in the complex plane (both operations have been performed with machine precision).

3. Q-FACTOR AND FREE-SPECTRAL RANGE INCREASE IN THE OPTIMALLY TUNED PHOTONIC MOLECULES

As mentioned in Section 1, microcavity-based sensors either detect the presence of a gas or an analyte in the cav-

ity cladding by measuring the resonant-mode wavelength shift (mass sensing) or measure the enhanced fluorescence from the cladding material at the resonant wavelength of the microcavity (fluorescence sensing). In both types of applications, a high value of the Q factor of the cavity mode used for detection is crucial for efficient and robust detection, as the resonance linewidth and the fluorescence enhancement effect are directly related to this value.

WG modes supported by microdisks are classified as $WG_{mn\ell}$ modes; m is the azimuthal number, n is the radial number, and ℓ is the vertical number. In thin disks considered in this paper, $\ell=1$ and will be omitted in the following discussion. Furthermore, only TE-polarized (having an electric field mostly in the cavity plane) modes will be considered, as in thin disks they have much larger effective refractive index values and are dominant.¹¹ Thus the field in the 2D setting is determined by a scalar principal vertical (out-of-plane) magnetic field component H_z . It is known that theoretical values of the Q factors of the circular microdisk WG modes grow exponentially with increased disk radius (increased modes azimuthal number).¹¹ This dependence is clearly observed in Fig. 3, where the Q factors of the WG modes in circular microdisks with increasing diameters are plotted. All the modes presented in Fig. 3 have resonant wavelengths around $\lambda = 1.55 \mu\text{m}$. However, such exponential Q factor growth is not observed in real-life microdisks, as high- Q values of higher-azimuthal-order modes are spoiled by the cavity sidewall surface roughness.^{2,21}

Another important cavity characteristic, the free-spectral range (FSR) or mode spectral spacing, is also plotted in Fig. 3. A large FSR value is especially important for the fluorescence sensing, as solvated fluorescent molecules usually have large emission bandwidths. Note that the cavity FSR should be much greater than the emission spectral width to yield the net fluorescence enhancement.^{9,22,23} Unlike the Q factors, the FSR values decrease with the increased cavity size (Fig. 3). It should also be noted that if the cavity surface roughness or coupling to a bus waveguide lifts the WG-mode degeneracy, the FSR values become much smaller.

Finally, it should be taken into account that the WG-mode interaction with the analyte occurs only through the

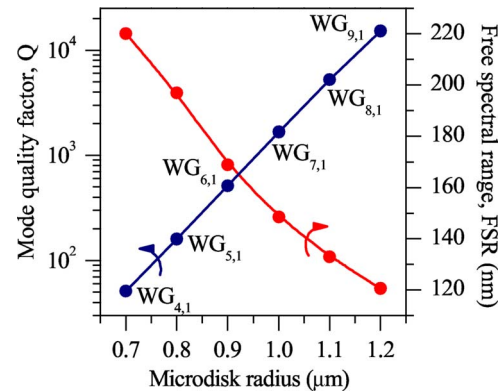


Fig. 3. (Color online) Values of the quality factors and FSRs of the WG modes in a 2D circular microdisk resonator ($n_{\text{eff}} = 2.63, n_e = 1.0$) with resonant wavelengths around $1.55 \mu\text{m}$ as a function of the disk radius. Note that all the modes are double degenerate owing to the disk symmetry.

evanescent portion of the mode field. The optical field of the high- Q WG modes is very efficiently confined in the microdisk, and therefore these modes are not very sensitive to the small changes in the microcavity environment. Near-field distributions (portraits of $|H_z(x,y)|$) of the $WG_{4,1}$ mode in a smaller $1.34\ \mu\text{m}$ diameter microdisk, and of the $WG_{7,1}$ mode in a larger $2\ \mu\text{m}$ diameter cavity are presented in Figs. 4(a) and 4(b), respectively. It can be clearly seen that the $WG_{4,1}$ -mode field extends much farther into the surrounding medium in the cavity plane. This presence of the region of relatively high-field intensity outside the cavity makes the cavity characteristics sensitive to the presence of the analyte in the cladding. At the same time, the poor mode confinement results in the very low $WG_{4,1}$ -mode Q -factor value, $Q=50.8$ (for comparison, the Q factors of the $WG_{7,1}$ mode is 1660).

To overcome this contradiction, this paper suggests arranging low- Q high-FSR nanocavities into predesigned symmetrical configurations supporting symmetry-enhanced photonic molecule supermodes with high- Q factors. For example, a square PM configuration has already been shown to offer a significantly (over 20 times) enhanced Q factors of the $WG_{6,1}$ molecule mode having odd field symmetry along the diagonals, and even symmetry along the x and y axes [OE mode].¹⁴ As demonstrated in Fig. 5, this Q factor boost can be achieved by optimally tuning the intercavity coupling distance. Figures 5(a) and 5(b) show the dependence of the resonant wavelength shifts and Q factor enhancements of three PM supermodes with four, six, and eight azimuthal field variations on the distance from the cavity centers to the PM center. Clearly, the lower the cavity azimuthal WG-mode number, the more sensitive it is to the presence of other cavities forming the photonic molecule. This higher sensitiv-

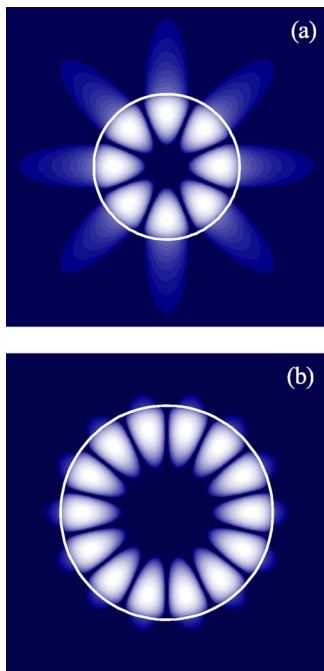


Fig. 4. (Color online) Magnetic near-field distributions of the WG modes in the vertical cross sections of two resonators: (a) $WG_{4,1}$ mode in a $1.34\ \mu\text{m}$ diameter disk and (b) $WG_{7,1}$ mode in a $2\ \mu\text{m}$ diameter disk.

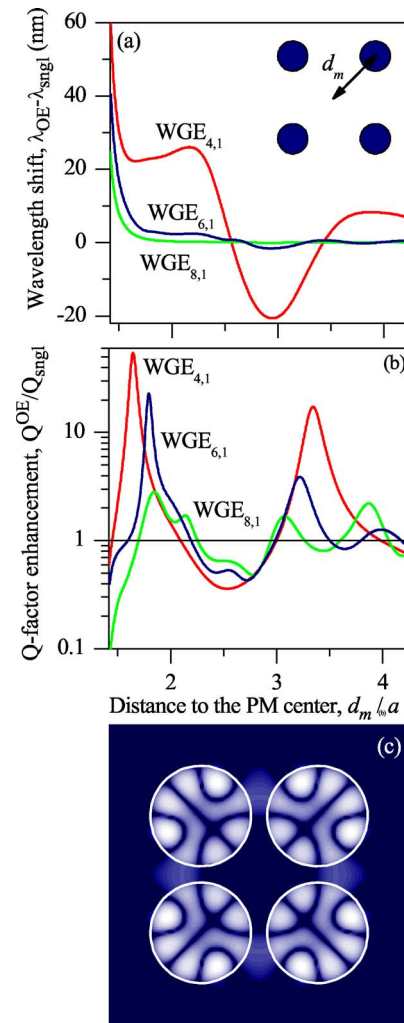


Fig. 5. (Color online) (a) Wavelength shifts and (b) Q -factor enhancements relative to corresponding single-cavity values of three OE supermodes of different azimuthal orders in a square PM versus distance d_m , and (c) near-field intensity distribution of the $WG_{4,1}$ OE supermode for $d_m=1.101\ \mu\text{m}$. The disk radii are $a=0.67, 0.9, \text{ and } 1.1\ \mu\text{m}$, respectively. The inset shows the PM geometry.

ity results in even more dramatic Q -factor enhancement (over 50 times) of the $WG_{4,1}$ supermode of OE symmetry ($Q^{\text{OE}}=2768$ for $d_m=1.101\ \mu\text{m}$). A near-field intensity portrait of the $WG_{4,1}$ OE supermode is shown in Fig. 5(c). It should also be noted that for this optimal PM configuration all the other closely located PM supermodes of different symmetries have Q -factor values many times lower, so that the PM free-spectral range is equal to that of a single cavity.

Next, in Fig. 6(a), we observe that arranging four optimally tuned PMs (with $d_m=1.101\ \mu\text{m}$) into a square configuration—we call it a photonic supermolecule (PSM)—and again adjusting the coupling distance d_s yields even further enhancement of the Q factor of the PSM OE supermode ($Q^{\text{OE}}=6656$ for $d_s=2.216\ \mu\text{m}$). The optimal configuration of the 16-cavity PSM together with the PSM OE supermode intensity portrait is shown in Fig. 6(b). Note that the PSM is not a periodic microdisk array but rather a fractallike structure; the distances between four PMs (d_s) and between four microdisks compos-

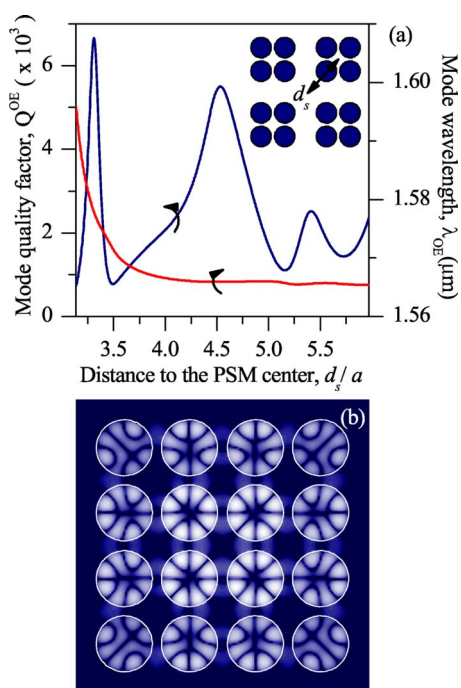


Fig. 6. (Color online) (a) Wavelength shift and Q -factor change of the $WG_{4,1}$ OE supermode in a square PSM versus distance d_s and (b) near-field intensity distribution of the $WG_{4,1}$ OE supermode in the optimally tuned PSM configuration with $d_s = 2.216 \mu\text{m}$.

ing each PM (d_m) have been tuned separately, and the intercavity separations are not identical for all the neighboring cavities. Once again, the FSR of the optimally tuned PSM is equal to its single-cavity counterpart.

4. SENSITIVITY ENHANCEMENT AT PHOTONIC MOLECULE RESONANCES

As PM modes are collective multicavity resonances, we expect their resonant frequencies to be more sensitive to changes in their environment (e.g., variations of the refractive index in the intercavity region) than the corresponding characteristics of a larger single cavity with a comparable value of the Q factor. In general, a microcavity configuration that provides a better overlap of the modal field with the analyte without degrading the mode Q factor should offer enhanced sensitivity.⁶

Now we compare the shifts of the resonant frequencies of a single microdisk WG mode and of the symmetry-enhanced OE supermodes of smaller-radius disks arranged into optimally tuned configurations caused by the change of the refractive index of the host medium. As a test single-cavity structure, we chose a $2 \mu\text{m}$ diameter microdisk resonator supporting a $WG_{7,1}$ mode with a Q -factor value ($Q = 1660$) of the same order as the PM OE-supermode Q factor. A $WG_{8,1}$ mode in a larger-radius microdisk will have a higher Q -factor value (see Fig. 3) but will be even less sensitive to the changes in the refractive index outside the resonator. As illustrated in Fig. 7(a), the cavity-mode wavelengths linearly shift to higher values as the refractive index value outside the resonator (i.e., gas or solution concentration) is increased. Clearly, the refractive index sensitivity [determined by the slope of the

lines in Fig. 7(a)] is enhanced for the PM-based sensor and even further enhanced for the PSM-based sensor. Also note [Fig. 7(b)] that although all the mode Q factors degrade slowly due to lowered index contrast between the microcavity and the cladding material, the PM and PSM Q factors remain higher than the single-cavity mode Q factor. It can also be expected that the increased overlap of the evanescent field of the high- Q PM and SPM modes with the surrounding medium would yield an enhanced performance of the biosensors based on the PMs immersed in a fluorophore solution.

Next, to calibrate the PM-based sensor for the detection of various solvents in the cladding of the structure, we consider a square PM consisting of the water-clad ($n = 1.333$) 200 nm thick, $1.3 \mu\text{m}$ diameter silicon disks ($n = 3.52$) located on a silica substrate ($n = 1.444$). The effec-

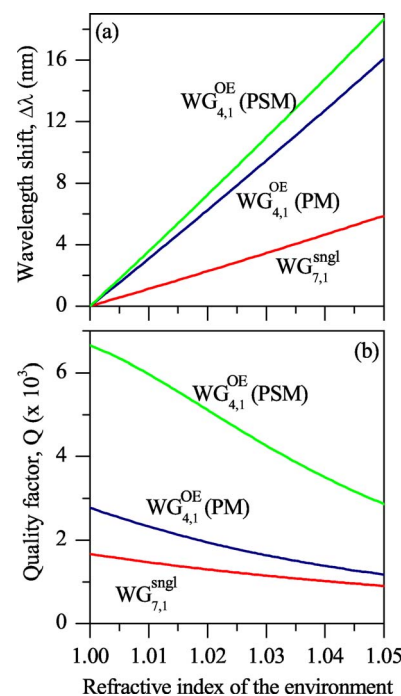


Fig. 7. (Color online) Comparison of (a) the wavelength shifts $\Delta\lambda = \lambda(n_e) - \lambda_0$ and (b) Q factors change as a function of the refractive index of the environment for a single $2 \mu\text{m}$ diameter microdisk operating on a $WG_{7,1}$ mode and for the PM and PSM operating on the symmetry-enhanced $WG_{4,1}$ OE supermodes.

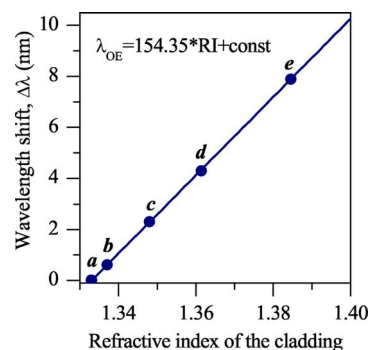


Fig. 8. (Color online) Calculated shifts of the PM $WG_{4,1}$ OE-supermode resonant wavelength as a function of the refractive index of the sensor cladding: (a) pure water, (b) 0.5% glucose, (c) 10% glucose, (d) EtOH, and (e) 1-propanol.

tive refractive index of the microcavities is $n_{\text{eff}}=2.813$. The optimally tuned PM configuration yielding the symmetry-enhanced $\text{WG}_{4,1}$ OE supermode corresponds to $d_s=1.078 \mu\text{m}$. As illustrated in Fig. 8, the resonant wavelength of the OE supermode of a photonic molecule systematically shifts to higher values with the increase of the refractive index of the solvent. The points on the plot correspond to the refractive indices of (a) pure water,³ (b) 0.5% glucose solution,²⁴ (c) 10% glucose solution, (d) EtOH,³ and (e) 1-propanol.²⁵ For example, changing the cladding refractive index from that of water ($n=1.3330$) to alcohol ($n=1.3614$) and to 1-propanol ($n=1.3845$) yields significant resonant wavelength upshifts of 4.28 and 7.88 nm, respectively (Fig. 8). Linear regression analysis yields a value of the refractive index unit (RIU) sensitivity of 153 nm RIU⁻¹. This theoretically predicted value of the refractive index sensitivity is of the same order as the experimentally reported typical sensitivity values of surface-plasmon biosensors based on individual chemically synthesized Ag nanoparticles (160–235 nm RIU⁻¹)²⁵ and as the values reported for nanolithography-fabricated Ag nanoparticle arrays (191 nm RIU⁻¹).²⁶ Note, however, that the Q factors of the surface-plasmon resonances on noble-metal nanoparticles are much lower than the corresponding values of the optical microcavity WG modes. For comparison, the measured refractive index sensitivity of a sensor based on a single Si_3N_4 circular microdisk resonator³ ($Q=4900$) is only 22.89 nm RIU⁻¹.

5. SINGLE-PARTICLE DETECTION

Finally, we explore a capability of the PM-based sensors to detect individual subwavelength-sized nanoparticles (note that conventional optical microscopy is limited to a spatial resolution of approximately 200 nm, or a half of the wavelength of visible light).²⁷ Similar to the cases of the mass or fluorescence sensing, the nanoparticle can interact with a microdisk or a PM mode field only through a small part of the mode expanding outside the resonator material as an evanescent field. This particle–WG-mode coupling results in a frequency shift of the mode that can be measured to detect the presence of the nanoparticle. Figure 9 presents wavelength shifts of the $\text{WG}_{4,1}$ OE su-

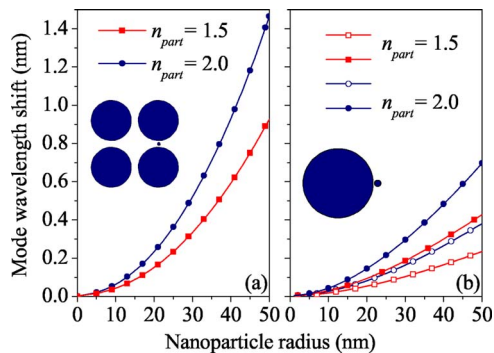


Fig. 9. (Color online) Comparison of the wavelength shifts of (a) the symmetry-enhanced PM $\text{WG}_{4,1}$ OE supermode and (b) of the single-disk $\text{WG}_{7,1}$ mode as a function of the radius of the detected nanoparticle. Degenerate microdisk mode splitting due to the presence of the nanoparticle is also observed in (b). The insets show the nanoparticle positions relative to the microresonator structures.

permode of a square photonic molecule [Fig. 9(a)] and of the $\text{WG}_{7,1}$ mode of a single microcavity [Fig. 9(b)] caused by a presence of a single nanoparticle as a function of the nanoparticle radius. Two circular-shaped dielectric nanoparticles are considered, with $n_{\text{part}}=1.5$ and $n_{\text{part}}=2$, and the microdisk and the PM parameters are the same as in Figs. 3–5. The nanoparticles are located either in between two neighboring cavities in the PM or at a 1 nm distance from the outer microdisk rim [nanoparticle positions relative to the sensors are shown in the insets to Figs. 9(a) and 9(b), respectively].

Mode wavelength shifts with the increased nanoparticle size are observed in both cases, though the PM supermode shows higher sensitivity to the presence of the nanoparticle. As could be expected, a higher-index nanoparticle causes more-significant mode frequency shifts of both structures. However, because the presence of the nanoparticle close to the microdisk sidewall disturbs the circular symmetry of the structure, not only shift but also splitting of the microdisk WG-mode frequency can be observed in Fig. 9(b). The wavelength spacing between the two split modes is approximately 0.2–0.3 nm, and this value drops rapidly with the increase of the nanoparticle–microcavity gap. Appearance of these two very closely located split modes with comparable Q factors will complicate the efficient detection of the nanoparticle. As the PM OE mode is nondegenerate, no mode splitting occurs in Fig. 9(a). Thus optimally tuned PM structures are expected to perform better than single microcavities in the sensor applications aimed at the detection of single nanoparticles such as proteins, antibodies, or viral particles as well as at the monitoring processes of synthesis and aggregation.²⁷

Finally, an accurate account for the evanescent-field interaction of a high- Q microcavity mode with a nanoparticle (or a fiber tip) provided by the developed theoretical framework is important for a variety of applications, including near-field microscopy,^{28,29} lasing with a single nanoemitter such as an individual nanocrystal or a quantum dot,³⁰ and the enhancement of single-molecule fluorescence.³¹ To correctly interpret the experimental results, the effect of the tip or the nanoemitter on the cavity-optical-mode frequency and Q factor has to be carefully evaluated. Furthermore, in all these applications, when a tip or a nanoemitter is placed in the evanescent-field region of the microcavity, it acts as a perturbing element that may yield degenerate cavity-mode splitting [Fig. 9(b)]. Thus optimally tuned quasi-single-mode PM structures studied in this paper would offer improved performance over conventional symmetrical cavity geometries, such as microdisks and microspheres.

6. FABRICATION TOLERANCES AND ON-CHIP INTEGRATION

To achieve the nanometer wavelength precision of high-index-contrast PM structures, nanometer geometry precision should be maintained. However, modern lithography techniques together with optimized etching processes enable the fabrication of wavelength-scale optoelectronic components such as photonic wire waveguides, microring and microdisk resonators, and photonic-crystal circuits

with very high and controllable precision.³² For example, isolated microdisks³³ and large regular microdisk arrays³⁴ with diameters of and below 2 μm have been fabricated with high structural and optical quality, and their experimentally measured WG-mode frequencies and Q factors have been reported to be remarkably close to the theoretical values predicted in the frame of simplified 2D models.^{16,18,33,34} Various techniques have also been developed for the reduction of the sidewall surface roughness (which is one of the principal sources of optical mode Q -factor degradation) such as, e.g., thermal oxidation of silicon-on-insulator photonic components.³⁵ Furthermore, lower-radial-order modes of smaller microdisks have been shown to exhibit better tolerance to the nanoscale surface roughness than high-radial-order, high- Q WG modes in larger resonators.²¹

Finally, by coupling optimally tuned PMs to bus waveguides, integrated semiconductor devices can be realized. In this case the C_{4v} symmetry of the structure may be distorted, which can result in degrading the Q factors of the PM supermodes. However, as has been previously demonstrated for square-microdisk optical waveguide filters, this loss of C_{4v} symmetry can be compensated and the high- Q factors maintained by slightly elongating the structure along the waveguide.³⁶

7. CONCLUSIONS

Summarizing, we proposed use of coupled-microdisk PMs that are tuned to support high- Q WG supermodes as a possible biochemical sensor platform. Such PMs can be efficiently designed with the rigorous analytical method and the numerical algorithm presented in this paper. It is theoretically demonstrated that the resonant wavelengths of the supermodes of optimal PM configurations are much more sensitive to the changes of the refractive index of their environment than single-cavity WG modes with comparable or even lower Q factors. Furthermore, PM-based sensors show promise in detecting individual nanoparticles with the sizes below the diffraction limit, such as viral particles and proteins. We attribute the demonstrated sensitivity enhancement to the increased overlap of the evanescent fields of the PM modes with the detected biological or chemical material.

S. Boriskina's e-mail address is SBoriskina@gmail.com.

REFERENCES

- R. W. Boyd and J. E. Heebner, "Sensitive disk resonator photonic biosensor," *Appl. Opt.* **40**, 5742–5747 (2001).
- E. Krioukov, D. J. W. Klunder, A. Driessen, J. Greve, and C. Otto, "Integrated optical microcavities for enhanced evanescent-wave spectroscopy," *Opt. Lett.* **27**, 1504–1506 (2002).
- E. Krioukov, D. J. W. Klunder, A. Driessen, J. Greve, and C. Otto, "Sensor based on an integrated optical microcavity," *Opt. Lett.* **27**, 512–514 (2002).
- C.-Y. Chao and L. J. Guo, "Biochemical sensors based on polymer microrings with sharp asymmetrical resonance," *Appl. Phys. Lett.* **83**, 1527–1529 (2003).
- F. Vollmer, S. Arnold, D. Braun, I. Teraoka, and A. Libchaber, "Multiplexed DNA quantification by spectroscopic shift of 2 microsphere cavities," *Biophys. J.* **85**, 1974–1979 (2003).
- J. Scheuer, W. M. J. Green, G. A. DeRose, and A. Yariv, "InGaAsP annular Bragg lasers: theory, applications, and modal properties," *IEEE J. Sel. Top. Quantum Electron.* **11**, 476–484 (2005).
- H. Quan and Z. Guo, "Simulation of whispering-gallery-mode resonance shifts for optical miniature biosensors," *J. Quant. Spectrosc. Radiat. Transf.* **93**, 231–243 (2005).
- W. Fang, D. B. Buchholz, R. C. Bailey, J. T. Hupp, R. P. H. Chang, and H. Cao, "Detection of chemical species using ultraviolet microdisk lasers," *Appl. Phys. Lett.* **85**, 3666–3668 (2004).
- S. Blair and Y. Chen, "Resonant-enhanced evanescent-wave fluorescence biosensing with cylindrical optical cavities," *Appl. Opt.* **40**, 570–582 (2001).
- H.-J. Moon, Y.-T. Chough, and K. An, "Cylindrical microcavity laser based on the evanescent-wave-coupled gain," *Phys. Rev. Lett.* **85**, 3161–3164 (2000).
- R. E. Slusher, A. F. J. Levi, U. Mohideen, S. L. McCall, S. J. Pearton, and R. A. Logan, "Threshold characteristics of semiconductor microdisk lasers," *Appl. Phys. Lett.* **63**, 1310–1312 (1993).
- M. Borselli, T. J. Johnson, and O. Painter, "Beyond the Rayleigh scattering limit in high- Q silicon microdisks: theory and experiment," *Opt. Express* **13**, 1515–1530 (2005).
- M. Bayer, T. Gutbrod, J. P. Reithmaier, A. Forchel, T. L. Reinecke, and P. A. Knipp, "Optical modes in photonic molecules," *Phys. Rev. Lett.* **81**, 2582–2586 (1998).
- S. V. Boriskina, "Theoretical prediction of a dramatic Q -factor enhancement and degeneracy removal of WG modes in symmetrical photonic molecules," *Opt. Lett.* **31**, 338–340 (2006).
- E. I. Smotrova, A. I. Nosich, T. M. Benson, and P. Sewell, "Threshold reduction in a cyclic photonic molecule laser composed of identical microdisks with whispering-gallery modes," *Opt. Lett.* **31**, 921–923 (2006).
- A. Nakagawa, S. Ishii, and T. Baba, "Photonic molecule laser composed of GaInAsP microdisks," *Appl. Phys. Lett.* **86**, 041112 (2005).
- A. L. Burin, H. Cao, G. C. Schatz, and M. A. Ratner, "High-quality optical modes in low-dimensional arrays of nanoparticles: application to random lasers," *J. Opt. Soc. Am. B* **21**, 121–131 (2004).
- S. V. Boriskina, P. Sewell, T. M. Benson, and A. I. Nosich, "Accurate simulation of 2D optical microcavities with uniquely solvable boundary integral equations and trigonometric-Galerkin discretization," *J. Opt. Soc. Am. A* **21**, 393–402 (2004).
- M. Abramovitz and I. Stegun, *Handbook of Mathematical Functions* (Dover, 1970).
- G. Tayeb and D. Maystre, "Rigorous theoretical study of finite-size two-dimensional photonic crystals doped by microcavities," *J. Opt. Soc. Am. A* **14**, 3323–3332 (1997).
- S. V. Boriskina, T. M. Benson, P. Sewell, and A. I. Nosich, "Spectral shift and Q change of circular and square-shaped optical microcavity modes due to periodical sidewall surface roughness," *J. Opt. Soc. Am. B* **21**, 1792–1796 (2004).
- H. Yokoyama and S. D. Brorson, "Rate equation analysis of microcavity lasers," *J. Appl. Phys.* **66**, 4801–4805 (1989).
- M. D. Barnes, W. B. Whitten, S. Arnold, and J. M. Ramsey, "Enhanced fluorescent yields through cavity quantum electrodynamic effects in microdroplets," *J. Opt. Soc. Am. B* **11**, 1297–1304 (1994).
- J. S. Maier, S. A. Walker, S. Fantini, M. A. Franceschini, and E. Gratton, "Possible correlation between blood glucose concentration and the reduced scattering coefficient of tissues in the near infrared," *Opt. Lett.* **19**, 2062–2064 (1994).
- A. D. McFarland and R. P. Van Duyne, "Single silver nanoparticles as real-time optical sensors with zeptomole sensitivity," *Nano Lett.* **3**, 1057–1062 (2003).
- M. D. Malinsky, K. L. Kelly, G. C. Schatz, and R. P. Van

- Duynne, "Chain length dependence and sensing capabilities of the localized surface plasmon resonance of silver nanoparticles chemically modified with alkanethiol self-assembled monolayers," *J. Am. Chem. Soc.* **123**, 1471–1482 (2001).
27. Z. Chen, A. Taflove, and V. Backman, "Photonic nanojet enhancement of backscattering of light by nanoparticles: a potential novel visible-light ultramicroscopy technique," *Opt. Express* **12**, 1214–1220 (2004).
28. S. Gotzinger, O. Benson, and V. Sandoghdar, "Influence of a sharp fiber tip on high- Q modes of a microsphere resonator," *Opt. Lett.* **27**, 80–82 (2002).
29. A. Giusto, S. Savasta, and R. Saija, "Interaction of a microresonator with a nanoscatterer," *J. Phys.: Conf. Ser.* **6**, 103–108 (2005).
30. M. Pelton and Y. Yamamoto, "Ultralow threshold laser using a single quantum dot and a microsphere cavity," *Phys. Rev. A* **59**, 2418–2421 (1999).
31. M. Steiner, F. Schleifenbaum, C. Stupperich, A. V. Failla, A. Hartschuh, and A. J. Meixner, "Microcavity-controlled single-molecule fluorescence," *ChemPhysChem* **6**, 2190–2196 (2005).
32. R. W. Boyd, J. E. Heebner, N. N. Lepeshkin, Q.-H. Park, A. Schweinsberg, G. W. Wicks, A. S. Baca, J. E. Fajardo, R. R. Hancock, M. A. Lewis, R. M. Boysel, M. Quesada, R. Welty, A. R. Bleier, J. Treichler, and R. E. Slusher, "Nanofabrication of optical structures and devices for photonics and biophotonics," *J. Mod. Opt.* **50**, 2543–2550 (2003).
33. T. Baba, M. Fujita, A. Sakai, M. Kihara, and R. Watanabe, "Lasing characteristics of GaInAsP–InP strained quantum-well microdisk injection lasers with diameter of 2–10 μm ," *IEEE Photon. Technol. Lett.* **9**, 878–880 (1997).
34. K. Petter, T. Kipp, Ch. Heyn, D. Heitmann, and C. Schuller, "Fabrication of large periodic arrays of AlGaAs microdisks by laser-interference lithography and selective etching," *Appl. Phys. Lett.* **81**, 592–594 (2002).
35. K. K. Lee, D. R. Lim, L. C. Kimerling, J. Shin, and F. Cerrina, "Fabrication of ultralow-loss Si/SiO₂ waveguides by roughness reduction," *Opt. Lett.* **26**, 1888–1890 (2001).
36. M. Lohmeyer, "Mode expansion modeling of rectangular integrated optical microresonators," *Opt. Quantum Electron.* **34**, 541–557 (2002).